The Astronomical Journal, 150:91 (16pp), 2015 September doi:10.1088/0004-6256/150/3/91

CHANDRA AND VERY LARGE ARRAY OBSERVATIONS OF THE NEARBY Sd GALAXY NGC 45

Thomas G. Pannuti[1], Douglas A. Swartz[2], Seppo Laine[3], Eric M. Schlegel[4], Christina K. Lacey[5], William P. Moffitt[1,6], Biswas Sharma[1,6], Aaron M. Lackey-Stewart[1], Alekzander R. Kosakowski[1,7], Miroslav D. Filipović[8], and Jeffrey L. Payne[8]
[1] Space Science Center, Department of Earth and Space Sciences, Morehead State University, 235 Martindale Drive, Morehead, KY 40351, USA; t.pannuti@moreheadstate.edu, wmoffitt@vols.utk.edu
[2] USRA/MSFC, 320 Sparkman Drive NW, Huntsville, AL 35805-1912, USA
[3] Spitzer Science Center, Mail Code 220-6, Caltech, Pasadena, CA 91125-0001, USA
[4] Department of Physics and Astronomy, University of Texas-San Antonio, 1 UTSA Circle, San Antonio, TX 78249-0600, USA
[5] Department of Physics and Astronomy, Hofstra University, 102 Berliner Hall, Hempstead, NY 11549, USA
[6] Department of Physics and Astronomy, University of Tennessee, 401 Nielsen Physics Building, 1408 Circle Drive. Knoxville, TN 37996-1200, USA
[7] Homer L. Dodge Department of Physics and Astronomy, University of Oklahoma, 440 W. Brooks Street, Norman, OK 73019, USA
[8] School of Computing, Engineering and Mathematics, University of Western Sydney, Locked Bag 1797, Penrith, NSW 2751, Australia
Received 2015 February 19; accepted 2015 July 2; published 2015 August 27

ABSTRACT

We present an analysis of high angular resolution observations made in the X-ray and the radio with the *Chandra X-ray Observatory* and the Karl Jansky Very Large Array (VLA), respectively, of the nearby spiral galaxy NGC 45. This galaxy is the third that we have considered in a study of the supernova remnant (SNR) populations of nearby spiral galaxies and the present work represents the first detailed analysis of the discrete X-ray and radio source populations of this galaxy. We analyzed data sets from the three pointed observations made of this galaxy with *Chandra* along with a merged data set obtained from combining these data sets: the total effective exposure time of the merged data set is 63515 s. A total of 25 discrete X-ray sources are found in the entire field of view of the ACIS-S3 chip, with 16 sources found within the visual extent of the galaxy. We estimate that as many as half of the sources detected in the entire field of view of the ACIS-S3 chip and seven of the sources detected in the optical extent of NGC 45 may be background sources. We analyzed the spectral properties of the discrete X-ray sources within the galaxy and conclude that the majority of these sources are X-ray binaries. We have searched for counterparts at different wavelengths to the discrete X-ray sources and we find two associations: one with a star cluster and the other with a background galaxy. We have found one source that is clearly variable within one observation and seven that are seen to vary from one observation to another. We also conduct a photometric analysis to determine the near-infrared fluxes of the discrete X-ray sources in *Spitzer* Infrared Array Camera channels. We constructed a cumulative luminosity function of the discrete X-ray sources seen toward NGC 45: taking into account simultaneously the luminosity function of background sources, the fitted slope of the cumulative luminosity function $\Gamma = -1.3^{+0.7}_{-1.6}$ (all error bounds correspond to 90% confidence intervals). The VLA observations reveal seven discrete radio sources: we find no overlaps between these sources and the X-ray detected sources. Based on their measured spectral indices and their locations with respect to the visible extent of NGC 45, we classify one source as a candidate radio SNR associated with the galaxy and the others as likely background galaxies seen in projection toward NGC 45. Finally, we discuss the properties of a background cluster of galaxies (denoted as CXOU J001354.2–231254.7) seen in projection toward NGC 45 and detected by the *Chandra* observations. The fit parameters to the extracted *Chandra* spectra of this cluster are a column density $N_{\rm H} = 0.07$ (<0.14) $\times 10^{22}$ cm^{-2}, a temperature $kT = 4.22^{+2.08}_{-1.42}$ keV, an abundance $Z = 0.30$(<0.75) relative to solar and a redshift $z = 0.28 \pm 0.14$. From the fit parameters we derive an electron number density $n_{\rm e} = 4(\pm 1) \times 10^{-3}$ cm^{-3}, an unabsorbed X-ray luminosity $L_{0.5-7.0\,\rm keV} \sim 8.77(\pm 0.96) \times 10^{43}$ erg s^{-1} for the cluster and an X-ray emitting mass $M = 2.32(\pm 1.75) \times 10^{12}\ M_{\odot}$.

Key words: galaxies: individual (NGC 45) – galaxies: spiral – ISM: supernova remnants – X-rays: binaries – X-rays: galaxies

1. INTRODUCTION

A lasting legacy of the *Chandra X-ray Observatory*—thanks to its unsurpassed angular resolution (approximately 1 arcsec resolution at 1 keV) and its outstanding flux sensitivity—has been its detection of large numbers of discrete X-ray sources in nearby galaxies (see Fabbiano 2006 for a review). The classes of discrete sources that are detected by pointed *Chandra* observations of nearby galaxies include central sources associated with galactic nuclei, resident supernova remnants (SNRs), X-ray binaries, and (due to projection effects) background galaxies. Examples of nearby galaxies that have been the subjects of such pointed observations with *Chandra* include M33 (Tuellmann et al. 2011), M51 (Terashima & Wilson 2004), M83 (Soria & Wu 2003), M101 (Pence et al. 2001) and NGC 2403 (Schlegel & Pannuti 2003).

In previous papers (Pannuti et al. 2000, 2002) we helped to establish the paradigm of using multi-wavelength observations to identify SNRs in nearby spiral galaxies (specifically NGC 300 and NGC 7793). Such studies of extragalactic SNRs offer the opportunity to investigate the properties of these sources in a manner that addresses the known observational obstacles encountered when studying Galactic SNRs. Specifically, these obstacles include considerable uncertainties in the distances to Galactic SNRs and significant absorption along the lines of

Table 1
General Properties of NGC 45

Property	NGC 45
R.A.[a] (J2000.0)	$00^h14^m04^s.0$
Decl.[a] (J2000.0)	$-23°10'55''$
Galactic Latitude b (°)	−80.67[a]
Galactic Longitude ℓ (°)	55.90[a]
Diameter D_{25} (arcmin)	8.3[b]
Axial Ratio d/D	0.73[b]
Column Density N_H (cm^{-2})	2.2×10^{20}[c]
Hubble Type[b]	SA(s)dm
Distance[d] (Mpc)	6.6
Inclination[b] i (°)	47

Notes.
[a] NED database.
[b] Tully (1988).
[c] Obtained from the Galactic neutral hydrogen density calculator (COLDEN)—available at http://cxc.harvard.edu/toolkit/colden.jsp.
[d] Jacobs et al. (2009).

sight to these sources (particularly at short wavelengths such as visible and X-ray), which limit thorough studies of Galactic SNRs to only those sources located in the neighborhood of the Sun (see Pannuti et al. 2007 for a more detailed review). Examples of papers that have provided detailed analysis of X-ray emission from samples of extragalactic SNRs as detected by *Chandra* include Long et al. (2010, 2014) who considered the SNRs located in the nearby spiral galaxies M33 and M83, respectively. Our prior analyses of *Chandra* observations of SNRs in nearby galaxies include the study of five galaxies in a flux-limited sample (Pannuti et al. 2007) as well as the study of the resident SNRs in NGC 7793 (Pannuti et al. 2011). In the present paper, we describe *Chandra* observations of another galaxy that were conducted to detect resident SNRs, namely the nearby spiral NGC 45.

In Table 1 we present a summary of the general properties of NGC 45. This galaxy has a remarkably low surface brightness and tepid star formation rate (SFR) (e.g., SFR = 0.40 $M_\odot$ yr^{-1}—see Lee et al. 2009) when compared to other nearby spiral galaxies. A rather low metallicity for NGC 45 has been reported in the literature as well: based on observations of the globular cluster population of the galaxy, Mora et al. (2008) measured an absorption line stellar abundance of 12 + log (O/H) = 8.5. The analysis presented in this paper therefore holds the potential of probing the discrete X-ray and radio source populations of a galaxy with a low SFR and a low metallicity.

The organization of this paper may be described as follows. In Section 2 we present the observations (and the accompanying data reductions) analyzed in this paper, namely the X-ray observations made with *Chandra* (Section 2.1) and the radio observations made with the Very Large Array (VLA) (Section 2.2). In addition to these X-ray and radio observations, we have also included infrared observations made of NGC 45 with *Spitzer* in the present study: we discuss these observations and the accompanying data reduction in Section 2.3. In Section 3, we present and describe the discrete X-ray and radio sources detected and considered in this paper. In turn, we discuss the properties of the discrete X-ray sources (Section 3.1), counterparts to these sources that are detected at other wavelengths (Section 3.2), the spectral properties of these sources (Section 3.3), a search for time-variability in the X-ray emission from the *Chandra*-detected sources (Section 3.4) and the infrared properties of the discrete X-ray sources (Section 3.5). We provide our own estimates of the SFR and the metallicity of NGC 45 in Section 4 while in Section 5 we analyze and describe the X-ray source luminosity function of the galaxy. The properties of a background galaxy cluster detected by these *Chandra*-observations—which we designate as CXOU J001354.2–231254.7—are discussed in Section 6 and the results of the radio observations of NGC 45 are given in Section 7. Lastly, in Section 8 we present the conclusions of this work. As is the case with many nearby galaxies, there have been a range of estimates of the distance to NGC 45 published in the literature. Chemin et al. (2009) provide a discussion of these published distance estimates and calculate a mean distance to NGC 45 of 5.9 Mpc based on these efforts. In the present paper, we will adopt a distance to NGC 45 of 6.6 Mpc as estimated by Jacobs et al. (2009) using the "tip of the red giant branch" method applied to a sample of nearby galaxies observed with the *Hubble Space Telescope*.

2. OBSERVATIONS AND DATA REDUCTION

2.1. Chandra Observations

The three observations of NGC 45 were made with the ACIS (Garmire et al. 2003) aboard the *Chandra X-ray Observatory* (Weisskopf 2002). The angular extent of NGC 45 (specifically the D_{25} isophote) was completely contained within the field of view of the ACIS-S3 chip, which itself has a field of view of $8\farcm3 \times 8\farcm3$. In Table 2 we present a summary of the *Chandra* observations of NGC 45. All of the observations were conducted in VERY FAINT mode. The effective exposure times of the three individual observations (ObsIDs 4690, 6184 and 6185) were 32860, 24641 and 6014 s, respectively, and the combined effective exposure time of the three observations was 63515 s.

The data sets were processed and reduced using standard tools in the *Chandra* Interactive Analysis of Observations (*CIAO*) Version 4.4 software package (Fruscione et al. 2006): the version of CALDB used in the analysis was 4.5.5.1. Each individual observation was reduced using the `chandra_repro` tool: this tool flags bad pixels and applies a time-dependent gain. Next, light curves were created to filter against background flares and generate good time intervals which were applied to each data set to complete the processing. The celestial locations of sources identified in all three event lists were compared and found to be in sufficient agreement (within one arcsec) to permit the combining of the three observations using the *CIAO* tool `merge_obs` without reprojection to produce a merged image. To detect individual discrete X-ray sources from the three individual observations as well as the merged observation, the *CIAO* tool `wavdetect` (Freeman et al. 2002) was used: this tool implements a "Mexican hat" wavelet function-based search algorithm that searches for correlations between the function and the given pixel scale size. A preliminary search for sources was conducted with `wavdetect` with the scale sizes set to 2.0 and 4.0 and the probability of a false detection set to 10^{-6}. A subsequent search for sources using larger scale sizes did not find any sources at a high statistical significance.

Table 2
Summary of *Chandra* Observations of NGC 45[a]

Sequence Number	ObsID	R.A. (J2000.0) (h m s)	Decl. (J2000.0) (° ′ ″)	Roll Angle (degrees)	Observation Date	Effective Exposure Time (s)
600345	4690	00:14:05.5	−23:12:54	283.01	2005 Jan 16	32860
600345	6184	00:14:05.5	−23:12:54	283.01	2005 Jan 12	24641
600345	6185	00:14:05.5	−23:12:54	283.01	2005 Jan 13	6014

Note.
[a] See Section 2.1.

2.2. Radio Observations

The radio data were collected in 1993 and 1994 using the VLA in spectral line mode, to allow wide field imaging without bandwidth smearing (chromatic aberration). See Table 3 for a summary of the radio observations made of NGC 45.

2.3. Infrared Observations

As part of this analysis, we used archival *Spitzer Space Telescope* images (Werner et al. 2004) of NGC 45 taken with the Infrared Array Camera (IRAC; Fazio et al. 2004) at 3.6, 4.5, 5.8 and 8.0 μm in the Local Volume Legacy Survey program (Dale et al. 2009) on 2007 December 26, consisting of eight 30 s frames (total maximum exposure per spatial position 214.4 s). The Basic Calibrated Data products (BCDs) are corrected for a gradient across the total imaged field of view before mosaicking. The *Spitzer* custom software MOPEX[9] is used for mosaicking, specifically the overlap and the mosaic routines. The final mosaic of the corrected BCD frames is constructed using the MOPEX mopex.pl script. Drizzle interpolation (drop factor of 0.75) was employed to determine the pixel values on a final grid of 0.75 arcsec pixel^{-1}, which is chosen to yield fully sampled images with maximal resolution.

Photometry was performed in the IRAC images using the elliptical Kron radius for the found objects in the output of SExtractor (Bertin & Arnouts 1996). For the X-ray source locations that did not have an infrared counterpart, we calculated an estimate by summing up the pixels in the continuous source area that were at least at the 2-σ level and subtracted an SExtractor-estimated background from them (typically at a level of 1/100th of the pixel values) and converted these from Jy pixel^{-1} to total flux values in μJy.

3. RESULTS: X-RAY PROPERTIES OF NGC 45

3.1. Discrete X-Ray Sources in NGC 45

In Table 4, we present a listing of the sources detected in the three individual observations (ObsIDs 4690, 6184 and 6185) and the merged observation of NGC 45, respectively. These observations detected totals of 14, 13, three and 24 sources, respectively, corresponding to a total of 25 unique X-ray sources. The coordinates of the sources, R.A. (J2000.0) and decl. (J2000.0), are given: we also list counterparts found for these sources and we discuss these counterparts in Section 3.2. A strong, extended X-ray source was also identified by eye in all observations: this source is the background galaxy cluster that is discussed in more detail in Section 6. In Table 5, we present count rates for all of the detected sources (as measured over the energy range of 0.5–7.0 keV) for the individual observations as well as for the merged observation. The sizes of the extraction regions used to find the numbers of counts per source were determined from `wavdetect`. No correction was made for flux falling outside the extraction region and the expected encircled flux fraction for the region size was 90%. Using the on-line tool PIMMS[10], we obtained conversion factors to be used to convert these count rates into absorbed and unabsorbed fluxes: from these fluxes, corresponding luminosities may be calculated. Adopting a power law model with a photon index $\Gamma = 1.8$ and a column density (corresponding to the Galactic column density toward NGC 45[11]) of $N_{\rm H} = 2.2 \times 10^{20}$ cm^{-2}, the conversion factors from count rates into absorbed and unabsorbed fluxes are 1.41×10^{11} and 1.36×10^{11} erg cm^{-2} s^{-1} counts^{-1} s, respectively. Using these conversion factors, the limiting unabsorbed luminosity attained by our observation of NGC 45 (for the assumed distance of 6.6 Mpc) is $\sim 10^{37}$ erg s^{-1}. In Figure 1 we present a *Spitzer* 8 μm infrared image of NGC 45 with the locations of all of the detected sources indicated. We discuss the properties of these discrete sources in the following subsections.

Table 3
NGC 45 Radio Observations[a]

Date	Frequency GHz	Array	Angular Resolution (arcsec)	rms Sensitivity/ Beam
1993 May 22	4.885	CnB	1.08	35.9 μJy/bm
1994 Jun 18	1.435	B	3.9	78 μJy/bm

Note.
[a] See Section 2.2.

For the sake of completeness, we extracted a spectrum of the diffuse X-ray emission from NGC 45 using the data set from the observation with the longest exposure time, namely ObsID 4690. The source extraction region corresponded to the full angular extent of the galaxy and excluded flux from the locations of the discrete sources identified by the CIAO tool `wavdetect` to minimize the effect of confusing flux from these sources. The signal-to-noise ratio of the spectrum was too poor for a detailed spectral analysis: we place an upper limit on the net count rate of 3.4×10^{-2} cts s^{-1} for the extracted spectrum over the energy range of 0.5–7.0 keV. Using PIMMS and adopting a thermal

[9] See http://irsa.ipac.caltech.edu/data/SPITZER/docs/dataanalysistools/tools/mopex/ for more information about this software package.

[10] See http://cxc.harvard.edu/toolkit/pimms.jsp.

[11] As indicated by the Galactic neutral hydrogen density calculator COLDEN —see http://cxc.harvard.edu/toolkit/colden.jsp.

Table 4
Summary of Detections of Sources and Counterparts in *Chandra* Observations of NGC 45[a]

Source	R.A. (J2000.0) (h m s)	Decl. (J2000.0) (° ′ ″)	Evans10	Liu11	Other Counterparts	Within Galaxy?
CXOU J001344.9–230856	00:13:44.9	–23:08:56.5	⋯	⋯	⋯	N
CXOU J001347.6–230739	00:13:47.6	–23:07:39.4	⋯	⋯	⋯	N
CXOU J001348.4–231029	00:13:48.4	–23:10:29.2	⋯	⋯	⋯	N
CXOU J001349.8–230857	00:13:49.8	–23:08:57.8	CXO J001349.9–230857	X9	⋯	Y
CXOU J001354.8–230723	00:13:54.8	–23:07:23.5	⋯	⋯	⋯	Y
CXOU J001356.0–231240	00:13:56.0	–23:12:40.4	CXO J001355.9–231240	X2	MRSS 473–113943?	Y
CXOU J001358.3–231107	00:13:58.3	–23:11:07.4	CXO J001358.2–231107	X10	⋯	Y
CXOU J001358.7–230639	00:13:58.7	–23:06:39.6	⋯	⋯	⋯	N
CXOU J001400.9–231017	00:14:00.9	–23:10:17.1	⋯	⋯	⋯	Y
CXOU J001401.2–230827	00:14:01.2	–23:08:27.9	CXO J001401.2–230828	X11	⋯	Y
CXOU J001403.0–231218	00:14:03.0	–23:12:18.9	CXO J001403.0–231218	X4	⋯	Y
CXOU J001403.6–231006	00:14:03.6	–23:10:06.9	CXO J001403.6–231006	X6	⋯	Y
CXOU J001404.1–231055	00:14:04.1	–23:10:55.3	CXO J001403.9–231055	X15	Nucleus, CL2_032?	Y
CXOU J001404.2–230746	00:14:04.2	–23:07:46.0	⋯	⋯	⋯	Y
CXOU J001404.6–231355	00:14:04.6	–23:13:55.2	⋯	⋯	⋯	Y
CXOU J001406.1–231006	00:14:06.1	–23:10:06.1	CXO J001406.1–231005	X7	⋯	Y
CXOU J001406.9–230707	00:14:06.9	–23:07:07.8	CXO J001406.8–230707	X3	⋯	N
CXOU J001409.8–230742	00:14:09.8	–23:07:42.3	⋯	⋯	⋯	N
CXOU J001410.6–230922	00:14:10.6	–23:09:22.3	⋯	⋯	⋯	Y
CXOU J001412.8–230911	00:14:12.8	–23:09:11.2	CXO J001412.7–230911	X19	⋯	Y
CXOU J001412.8–231111	00:14:12.8	–23:11:11.8	⋯	⋯	⋯	Y
CXOU J001413.6–230831	00:14:13.6	–23:08:31.3	CXO J001413.7–230830	⋯	⋯	N
CXOU J001413.8–231355	00:14:13.8	–23:13:55.1	⋯	⋯	⋯	Y
CXOU J001419.7–231309	00:14:19.7	–23:13:09.3	CXO J001419.6–231309	X12	⋯	N
CXOU J001420.4–231235	00:14:20.4	–23:12:35.0	CXO J001420.3–231235	X8	⋯	N

Notes.
[a] See Sections 3.1 and 3.2. Counterparts identified using a 5 arcsec search radius. Evans10—from Evans et al. (2010). Liu11—from Liu (2011). MRSS—background galaxy detected by the Muenster Red Sky Survey (Ungruhe et al. 2003). CL—resident star cluster detected by Silva-Villa & Larsen (2011).

plasma model (namely the APEC model, where APEC stands for Astrophysical Plasma Emission Code—see Smith et al. 2001 and Foster et al. 2012) with a column density $N_{\rm H} = 2.2 \times 10^{20}$ cm^{-2} and an elemental abundance of 0.6 solar, this upper limit on the count rate corresponds to a limiting unabsorbed flux of 1.4×10^{-13} erg cm^{-2} s^{-1} or a corresponding limiting surface brightness of 4.3×10^{-15} erg cm^{-2} s^{-1} arcmin^{-2}. This surface brightness value is roughly comparable to the surface brightness of the diffuse X-ray background of $\sim$4–5 $\times 10^{-15}$ erg cm^{-2} s^{-1} arcmin^{-2} as measured by Markevitch et al. (2003). We therefore place an upper limit on the luminosity of the diffuse X-ray emission from NGC 45 (integrated over the entire spatial extent of the galaxy) of $\sim 1.2 \times 10^{39}$ erg s^{-1} over the 0.5–7.0 keV energy range.

3.2. Counterparts to Discrete X-Ray Sources Detected At Other Wavelengths

Previous X-ray observations: before the *Chandra* observations of NGC 45 that we consider in this paper were presented, there had been no pointed observations made of this galaxy with another X-ray observatory. Prior analyses of the *Chandra* observations discussed in this paper were presented by Evans et al. (2010) and Liu (2011). As part of their creation of the *Chandra* Source Catalog (CSC),[12] Evans et al. (2010) identified eighteen discrete X-ray sources within a radius of 4.4 arcmin of the nominal center of NGC 45 as detected by these observations. Similarly, Liu (2011) analyzed these observations as part of a study of the discrete X-ray source population in a sample of 383 nearby galaxies as detected by *Chandra*. In analyzing the same three observations that we have considered, Liu (2011) cataloged a total of 20 sources as detected on the ACIS-S2 chip as well as the ACIS-S3 chip. As part of our analysis, we searched for overlaps between our sample of sources and the samples of sources given by Evans et al. (2010) and Liu (2011).

We first compared our sample of sources with the sample of sources listed in the CSC: of the eighteen sources listed in that sample, we have found counterparts to thirteen of them. The remaining five sources are associated with the extended diffuse emission of the background galaxy cluster. We then compared our sample of sources to the sample published by Liu (2011): we found thirteen of the 20 sources in that sample: we note that the eleven sources found by CSC were also found by Liu (2011) as well as us. Of the remaining seven sources of Liu (2011) that we did not detect, four (X1, X5, X13 and X14) were detected on the ACIS-S2 chip while the remaining three (X16, X17 and X18) were not detected by us: a visual inspection of the putative locations of these sources did not reveal any obvious emission. We note that one of the sources we found in common with Liu (2011)—namely X20—is the background galaxy cluster: we will discuss this source in more detail in Section 6. We find twelve discrete sources that were not detected by either Evans et al. (2010) or Liu (2011): all of these sources are detected close to our threshold of detection ($\sim 3 \times 10^{-4}$ cts s^{-1}) and additional sensitive X-ray observations are required to detect these sources more robustly. In Table 4

[12] See http://cxc.harvard.edu/csc for more information about the CSC.

Table 5
Summary of Count Rates of Detected Sources in *Chandra* Observations of NGC 45[a]

Source	ObsID 4690 Count Rate (counts s^{-1})	ObsID 6184 Count Rate (counts s^{-1})	ObsID 6185 Count Rate (counts s^{-1})	Merged Observation Count Rate (counts s^{-1})
CXOU J001344.9–230856	⋯	⋯	⋯	$4.46(\pm0.83) \times 10^{-4}$
CXOU J001347.6–230739	⋯	⋯	⋯	$3.38(\pm0.72) \times 10^{-4}$
CXOU J001348.4–231029	⋯	$3.25(\pm1.61) \times 10^{-4}$ (2)	⋯	$3.38(\pm0.72) \times 10^{-4}$
CXOU J001349.8–230857	$1.45(\pm0.21) \times 10^{-3}$ (2)	$1.34(\pm0.23) \times 10^{-3}$ (0)	⋯	$1.47(\pm0.15) \times 10^{-3}$
CXOU J001354.8–230723	⋯	⋯	⋯	$3.69(\pm0.75) \times 10^{-4}$
CXOU J001356.0–231240	$4.39(\pm0.36) \times 10^{-3}$ (0)	$3.90(\pm0.40) \times 10^{-3}$ (0)	$2.83(\pm0.87) \times 10^{-3}$ (0)	$3.98(\pm0.25) \times 10^{-3}$
CXOU J001358.3–231107	$4.94(\pm1.51) \times 10^{-4}$ (0)	$8.93(\pm1.90) \times 10^{-4}$ (0)	⋯	$6.76(\pm0.10) \times 10^{-4}$
CXOU J001358.7–230639	⋯	⋯	⋯	$3.07(\pm0.69) \times 10^{-4}$
CXOU J001400.9–231017	⋯	⋯	⋯	$2.94(\pm1.34) \times 10^{-4}$
CXOU J001401.2–230827	$4.94(\pm1.51) \times 10^{-4}$ (0)	$4.46(\pm1.80) \times 10^{-4}$ (0)	⋯	$5.84(\pm0.95) \times 10^{-4}$
CXOU J001403.0–231218	$2.35(\pm0.26) \times 10^{-3}$ (0)	$2.96(\pm0.35) \times 10^{-3}$ (0)	$2.49(\pm0.83) \times 10^{-3}$ (0)	$2.64(\pm0.20) \times 10^{-3}$
CXOU J001403.6–231006	$1.48(\pm0.21) \times 10^{-3}$ (0)	$1.91(\pm0.28) \times 10^{-3}$ (0)	$1.33(\pm0.66) \times 10^{-3}$ (0)	$1.67(\pm0.16) \times 10^{-3}$
CXOU J001404.1–231055	$3.78(\pm1.38) \times 10^{-4}$ (0)	$2.43(\pm1.46) \times 10^{-4}$ (0)	⋯	$2.77(\pm0.82) \times 10^{-4}$
CXOU J001404.2–230746	⋯	⋯	⋯	$4.46(\pm0.83) \times 10^{-4}$
CXOU J001404.6–231355	$3.19(\pm1.29) \times 10^{-4}$ (2)	⋯	⋯	⋯
CXOU J001406.1–231006	$1.71(\pm0.22) \times 10^{-3}$ (0)	$1.02(\pm0.20) \times 10^{-3}$ (1)	⋯	$1.41(\pm0.15) \times 10^{-3}$
CXOU J001406.9–230707	$1.95(\pm0.24) \times 10^{-3}$ (6)	$2.76(\pm0.33) \times 10^{-3}$ (0)	⋯	$2.63(\pm0.20) \times 10^{-3}$
CXOU J001409.8–230742	⋯	⋯	⋯	$3.38(\pm0.72) \times 10^{-4}$
CXOU J001410.6–230922	⋯	⋯	⋯	$3.69(\pm0.75) \times 10^{-4}$
CXOU J001412.8–230911	$4.36(\pm1.44) \times 10^{-4}$ (2)	⋯	⋯	$3.23(\pm0.70) \times 10^{-4}$
CXOU J001412.8–231111	⋯	$2.03(\pm1.38) \times 10^{-4}$ (0)	⋯	$2.92(\pm0.84) \times 10^{-4}$
CXOU J001413.6–230831	⋯	⋯	⋯	$4.30(\pm0.81) \times 10^{-4}$
CXOU J001413.8–231355	$2.03(\pm1.10) \times 10^{-4}$ (1)	⋯	⋯	$2.77(\pm0.82) \times 10^{-4}$
CXOU J001419.7–231309	$8.42(\pm1.56) \times 10^{-4}$ (0)	$6.49(\pm1.62) \times 10^{-4}$ (1)	⋯	$8.30(\pm1.13) \times 10^{-4}$
CXOU J001420.4–231235	$7.26(\pm1.45) \times 10^{-4}$ (0)	$9.74(\pm1.99) \times 10^{-4}$ (0)	⋯	$7.83(\pm0.11) \times 10^{-4}$

Notes.
[a] Count rates may be converted from counts per second into absorbed and unabsorbed luminosities (in units of erg cm^{-2} s^{-1}) using the conversion factors of 1.41×10^{11} and 1.36×10^{11} erg cm^{-2} s^{-1} $counts^{-1}$ s, respectively. These physical parameters are determined assuming a power law model with a photon index $\Gamma = 1.8$ and a foreground column density $N_H = 2.2 \times 10^{20}$ cm^{-2} for a Cycle 5 observation. The quantity given in parenthesis is the variability index as measured using the CIAO tool `glvary`. See Sections 3.1 and 3.4.

we list the associations between our detected sources and the sources found by Evans et al. (2010) and Liu (2011).

Below we outline our search for counterparts at other wavelengths to the discrete X-ray sources detected by *Chandra*. We have used a generous search radius of 5 arcsec to identify possible counterparts to these X-ray sources: a summary of our search for counterparts is presented in Table 4.

Foreground stars: two particularly bright foreground stars (with apparent magnitudes $m_V < 10$) are seen in projection toward NGC 45.[13] We have searched for associations between our detected X-ray sources and foreground stars (including these two bright foreground stars) and we find no associations.

Star clusters: a search was made to identify X-ray counterparts to star clusters identified in this galaxy by Silva-Villa & Larsen (2011). We found one such possible association: it is between the detected X-ray source CXOU J001404.1–231055 and the cluster CL 2_032. We note that the location of this X-ray source toward the nucleus of NGC 45 (and thus a region of significant visible confusion) must be taken into account when determining if the association between this X-ray source and the star cluster is genuine.

SNRs: there has been a prior optical search for SNRs in NGC 45 by Dodorico et al. (1980). This search made use of narrow-band [S II] and Hα images of the galaxy: SNRs manifest themselves as sources for which the ratio of the summed flux for the two lines of the forbidden transition [S II] doublet at 671.7 and 673.1 nm to the ratio of the flux of the Hα line at 656.3 nm equals or exceeds 0.4. In contrast, for sources with similar diffuse morphologies as SNRs (like planetary nebulae and H II regions) the observed values for this ratio are 0.2 or less. The origin of the differences in the values for this ratio may be traced to gas associated with SNRs experiencing a single collisional-ionization event from the SNR shock (thus most sulfur atoms in the gas are singly ionized) while the gas associated with planetary nebulae and H II regions is subject to continuous photo-ionization (thus most sulfur atoms in the gas are multiply ionized). Thus, the [S II]/Hα ratio may serve as an effective discriminant in distinguishing SNRs from other sources with similar diffuse morphologies in nearby galaxies through optical searches. The reader is referred to Blair & Long (1997), Matonick & Fesen (1997) and Blair & Long (2004) for more information about optical searches using this ratio to identify SNRs in nearby galaxies.

[13] One star—seen toward the southwest of the disk of the galaxy—is HD 941 (SAO 166132): the apparent magnitude of this star is $m_V = 6.87$, the coordinates of this star are R.A. (J2000.0) $00^h13^m45^s.498$, decl.(J2000.0) $-23°12'53''.2$ and the spectral type of this star is K1IIICNv. The second star—seen just south of the nucleus of NGC 45—is CD-23 55 (SAO 166133): the apparent magnitude of this star is $m_V = 9.88$, the coordinates of this star are R.A. (J2000.0) $00^h14^m05^s.526$, decl.(J2000.0) $-23°12'26''.58$ and the spectral type of this star is K0.

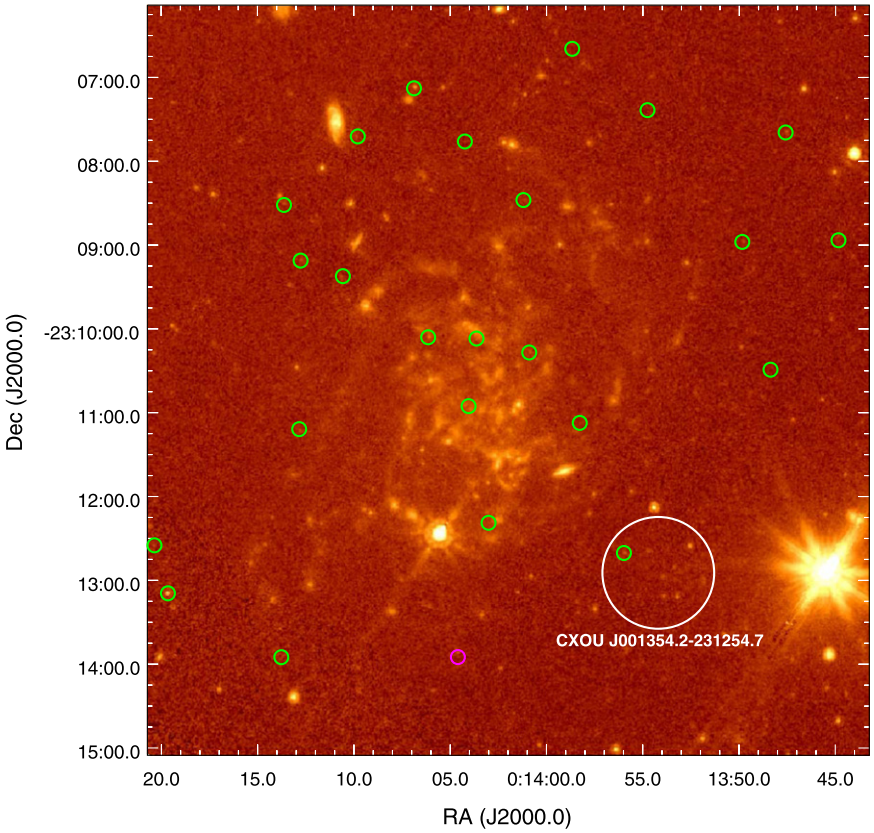

Figure 1. 8 μm image of NGC 45 taken by the Infrared Array Camera (IRAC) aboard the *Spitzer Infrared Space Telescope*. The green circles indicate the locations of sources detected by the merged observation while the magenta circle corresponds to source CXOU J001404.6–231355, the source that was detected in the ObsID 4690 observation but not in the merged observation. The location of the background galaxy cluster CXOU J001354.2-231254.7 is indicated with a white circle with a radius of 40 arcsec corresponding to the radius of the X-ray spectral extractions. See also Sections 3 and 6.

In their survey, Dodorico et al. (1980) failed to detect any SNRs in NGC 45. We have conducted our own multi-wavelength search for SNRs in NGC 45 as a way to extend the initial work of Dodorico et al. (1980). Using the set of discrete X-ray sources detected by *Chandra*, we first searched for positional associations between the detected X-ray sources with regions of diffuse optical emission associated with NGC 45. To help reduce confusion with X-ray sources of other types (such as X-ray binaries resident to NGC 45), we considered only those X-ray sources with soft spectra as indicated by the quantile analysis performed on the spectra of these sources and described in Section 3.3. Such soft X-ray spectra would be produced by a source with shock-heated gas and emitting thermal bremsstrahlung radiation (like an SNR) while harder X-ray spectra may be produced by different classes of sources (such as X-ray binaries or background galaxies). We find no overlaps between sources with soft X-ray spectra and regions of diffuse emission: in Section 7, we describe our search for SNRs in NGC 45 using radio observations. We note that it is not surprising that any resident SNRs in NGC 45 were undetected in the X-ray. In our previous analysis of a *Chandra* observation of the nearby galaxy NGC 7793 (Pannuti et al. 2011), we attained approximately the same limiting unabsorbed luminosity as that attained by the present study of NGC 45 and we found few X-ray SNRs in NGC 7793. As noted in that paper, only about ten Galactic SNRs are known to have X-ray luminosities that exceed the limiting luminosity of our observation[14], though comparisons with the Galactic SNR population need to be tempered by the fact that significant absorption along Galactic lines of sight causes many soft X-ray emitting sources like SNRs to remain undetected. In their study of X-ray emission from SNRs in the galaxy M83, Long et al. (2014) estimated a surface area distribution of the SNRs to be approximately 1000 SNRs per square degree at a flux limit corresponding to that attained by our observation of NGC 45. For our source with the angular extent of NGC 45, we would expect to detect approximately 11 SNRs, but the SFR of M83 is an order of magnitude greater than that of NGC 45 (for example, Karachentsev & Kaisinia 2013 and Karachentsev et al. 2013 estimate the SFRs of NGC 45 and M83 to be 0.55 and 2.82 $M_{\odot}$ yr^{-1}, respectively, based on Hα fluxes of the galaxies). Assuming that the SNR detection rate of a galaxy scales in proportion to its SFR, from the estimate of Long et al. (2014) we may expect to detect only one SNR in the X-ray in NGC 45, which broadly matches our result. The low SFR of NGC 45 (as calculated and discussed in Section 4) suggests that both the sheer number of SNRs and the number of luminous SNRs is probably much lower than in galaxies like the Milky Way and NGC 7793 that have much higher SFRs.

Background galaxies: we considered the 26 background quasars seen in projection toward NGC 45 by the visible survey conducted by Crampton et al. (1997): we find no associations between our detected discrete X-ray sources and those quasars. Using the NASA Extragalactic Database (NED)[15], we searched

[14] See "The *Chandra* Supernova Remnant Catalog" (http://hea-www.harvard.edu/ChandraSNR).

[15] See http://nedwww.ipac.caltech.edu.

for other known external galaxies that could be counterparts to the detected X-ray sources. We found one such possible counterpart to a detected X-ray source, namely the galaxy MRS 473–113943 as identified by the Muenster Red Sky Survey (Ungruhe et al. 2003).

We estimate the number of detected background sources that are seen in projection beyond NGC 45 using the relation given by Campana et al. (2001): we express the relevant quantity N (the number of background sources greater than a flux density S per square degree) as (in CGS units)

$$Nc(>S) = 360 \times \left(\frac{S}{2 \times 10^{-15}}\right)^{-0.68}, \quad (1)$$

where the bandpass over which S is measured is 0.5–2.0 keV. For our merged image, we estimate that the limiting flux density (using the model parameters described in Section 3.1) to be 6.38×10^{-16} erg cm^{-2} s^{-1}: therefore from Equation (1) we calculate 783 X-ray sources will be detected per square degree. This corresponds to fifteen sources within the field of view of the ACIS-S3 chip: therefore about 60% of the sources that we detect may be background objects. Among the 16 sources found within the visible extent of NGC 45, from Equation (1) we calculate that approximately seven of these 16 sources may be background objects.

3.3. Spectral Properties of Discrete X-Ray Sources

We adopted the quantile approach to a color–color diagram (Hong et al. 2004). The quantile method determines the energy below which a specified percentage of events falls. Colors are determined by ratios or differences of the resulting energies. Instead of an orthogonal grid as built for a hardness ratio, the interpretative grid has a compressed appearance. The compressed appearance reflects the true spectral energy information available from the instrument for a given spectral model. We have used this approach previously in our prior analysis of a *Chandra* observation of the galaxy NGC 7793 (Pannuti et al. 2011). Quantiles are discussed in detail by Hong et al. (2004) and we present a brief summary here. A quantile Q_X may be described as follows: first we define E_X as the energy below which the net counts are X% of the total net counts. Therefore, E_{25}, E_{50} and E_{75} correspond to the energies below which the counts are 25%, 50% and 75%, respectively. Thus, we may define Q_X as

$$Q_X = \frac{E_X - E_{\rm low}}{E_{\rm high} - E_{\rm low}}. \quad (2)$$

Here, $E_{\rm low}$ and $E_{\rm high}$ are the lower and upper boundary energies, respectively, of the full energy band considered: in the present paper, we have adopted values of $E_{\rm low} = 0.5$ keV and $E_{\rm high} = 7.0$ keV. To help maximize the separation of the data and to be consistent with the previous work presented in Pannuti et al. (2011), we define a grid with $3 \times (Q_{25}/Q_{75})$ versus log $(Q_{50}/(1\text{-}Q_{50}))$.

Our calculated quantile values for the sources detected with count rates of 10^{-3} cts s^{-1} or greater—in the three individual observations and in the merged observation—are presented in Table 6. In Figures 2 and 3 we present the quantile grids for the power law and bremsstrahlung models, respectively. For both grids, moving quasi-vertically in the grid crosses lines of equal $N_{\rm H}$ with values of 0.001 (bottom), 0.005, 0.01, 0.05, 0.1, 0.5, and 1.0×10^{22} cm^{-2} (top). Moving horizontally crosses lines of equal continuum parameter (e.g., temperature (bremsstrahlung) or power law index).

The foreground $N_{\rm H}$ is $\sim 2.2 \times 10^{20}$ cm^{-2} and corresponds approximately to a line of constant $3 \times \frac{Q_{25}}{Q_{75}}$ of 0.6–0.7. Hence, the "cloud" of data points near (0.75, 0.75) is consistent with the column density toward NGC 45. Given their position, their implied spectra are rather hard so these objects are then candidate X-ray binaries or background active galactic nuclei (AGNs).

Of interest are the variations among the three epochs. Three detected sources (namely CXOU J001356.0–231240, CXOU J001403.6–231006 and CXOU J001406.9–230707) appear to be significantly spectrally variable: this variability is exhibited by the changes in locations of the plotted positions of these sources in Figures 2 and 3. Specifically, two sources (CXOU J001403.6–231006 and CXOU J001406.9–230707) show an increase in absorption through the observation while the third (CXOU J001356.0–231240) appears to soften.

3.4. Variability in the X-Ray Emission from the Detected Sources

The CIAO tool `glvary` was used to check the variability of the detected sources in each observation. This tool uses the Gregory–Loredo variability test (Gregory & Loredo 1992) algorithm to first bin the events based on time and then to conduct a search for deviations within those binnings.[16] The tool calculates a variability index based on this search for deviations within the binnings: this index may be interpreted such that a value of 0, 1, 2, 3, 4, 5 and 6 through 10 indicates that source definitely is not variable, is considered to not be variable, is probably not variable, may be variable, is likely to be variable, is considered to be variable and is definitely variable, respectively. Table 5 contains all of the variability indices for the three observations of NGC 45. Only one source (CXOU J001406.9–230707) was found to be variable during the course of a single observation: the `glvary` tool returned a variability index of 6 for the source during the ObsID 4690 observation. Inspection of an visual image at the location of this source reveals no obvious counterpart: we also find no counterpart to this source at any wavelength. Such a source may be a background galaxy seen through the disk of the galaxy or an X-ray binary physically associated with NGC 45 itself.

We have searched for variability in the X-ray emission from the detected sources between the three different observations. We first compared the two longer exposure observations (ObsIDs 4690 and 6184): the difference between the effective exposure times of the two observations is approximately 10 ks, which leads to a difference in flux sensitivity that must be taken into account. In comparing the sets of sources detected by the two observations and the measured count rates of the same source, we find that seven sources do in fact show a detectable change in brightness (at the 90% confidence level) from the first observation to the second. Regarding the third observation (ObsID 6185), which has an order of magnitude shorter exposure time than the other two observations, it has limited ability to constrain the variability of the discrete sources and

[16] See http://cxc.harvard.edu/ciao/ahelp/glvary.html for more information about this tool.

Table 6
Quantile Values For Individual Observations and Merged Observation[a]

Source	Q_{25}	Q_{50}	Q_{75}	log $(Q_{50}/(1\text{-}Q_{50}))$	$3Q_{25}/Q_{75}$
			ObsID 4690		
CXOU J001349.8–230857	0.09 ± 0.02	0.16 ± 0.03	0.35 ± 0.08	$-0.72^{+0.09}_{-0.10}$	0.75 ± 0.17
CXOU J001356.0–231240	0.08 ± 0.01	0.14 ± 0.01	0.28 ± 0.04	$-0.78^{+0.04}_{-0.05}$	0.85 ± 0.12
CXOU J001403.0–231218	0.09 ± 0.01	0.16 ± 0.01	0.33 ± 0.06	−0.72 ± 0.04	0.78 ± 0.15
CXOU J001403.6–231006	0.07 ± 0.02	0.14 ± 0.01	0.19 ± 0.06	$-0.78^{+0.04}_{-0.05}$	1.03 ± 0.34
CXOU J001406.1–231006	0.07 ± 0.01	0.14 ± 0.02	0.28 ± 0.05	$-0.79^{+0.08}_{-0.10}$	0.70 ± 0.14
CXOU J001406.9–230707	0.14 ± 0.01	0.19 ± 0.02	0.35 ± 0.04	$-0.62^{+0.06}_{-0.07}$	1.16 ± 0.12
			ObsID 6184		
CXOU J001349.8–230857	0.11 ± 0.02	0.21 ± 0.03	0.44 ± 0.10	$-0.59^{+0.08}_{-0.09}$	0.73 ± 0.17
CXOU J001356.0–231240	0.06 ± 0.01	0.15 ± 0.03	0.33 ± 0.06	$-0.75^{+0.10}_{-0.12}$	0.58 ± 0.09
CXOU J001403.0–231218	0.08 ± 0.01	0.13 ± 0.02	0.23 ± 0.03	$-0.84^{+0.08}_{-0.10}$	1.03 ± 0.16
CXOU J001403.6–231006	0.09 ± 0.02	0.18 ± 0.04	0.37 ± 0.08	$-0.66^{+0.10}_{-0.12}$	0.70 ± 0.16
CXOU J001406.1–231006	0.12 ± 0.02	0.15 ± 0.04	0.50 ± 0.16	$-0.76^{+0.13}_{-0.16}$	0.69 ± 0.20
CXOU J001406.9–230707	0.12 ± 0.02	0.25 ± 0.04	0.47 ± 0.04	$-0.49^{+0.09}_{-0.10}$	0.78 ± 0.11
			ObsID 6185		
CXOU J001356.0–231240	0.07 ± 0.03	0.12 ± 0.06	0.25 ± 0.20	$-0.88^{+0.20}_{-0.31}$	0.81 ± 0.56
CXOU J001403.0–231218	0.12 ± 0.04	0.17 ± 0.07	0.39 ± 0.11	$-0.68^{+0.18}_{-0.25}$	0.89 ± 0.32
CXOU J001403.6–231006	0.03 ± 0.01	0.05 ± 0.02	0.08 ± 0.06	$-1.31^{+0.21}_{-0.38}$	1.05 ± 0.64
			Merged		
CXOU J001349.8–230857	0.10 ± 0.01	0.17 ± 0.02	0.37 ± 0.06	$-0.69^{+0.06}_{-0.07}$	0.82 ± 0.13
CXOU J001356.0–231240	0.07 ± 0.01	0.14 ± 0.01	0.29 ± 0.04	$-0.79^{+0.04}_{-0.05}$	0.71 ± 0.09
CXOU J001358.3–231107	0.08 ± 0.02	0.19 ± 0.04	0.36 ± 0.12	$-0.65^{+0.11}_{-0.13}$	0.64 ± 0.21
CXOU J001403.0–231218	0.09 ± 0.01	0.16 ± 0.01	0.27 ± 0.03	−0.74 ± 0.04	0.95 ± 0.12
CXOU J001403.6–231006	0.07 ± 0.01	0.14 ± 0.01	0.24 ± 0.05	−0.08 ± 0.05	0.83 ± 0.18
CXOU J001406.1–231006	0.08 ± 0.01	0.15 ± 0.02	0.31 ± 0.06	$-0.77^{+0.05}_{-0.06}$	0.72 ± 0.14
CXOU J001406.9–230707	0.13 ± 0.01	0.23 ± 0.01	0.39 ± 0.03	−0.53 ± 0.03	1.04 ± 0.08
CXOU J001420.4–231235	0.19 ± 0.02	0.30 ± 0.05	0.53 ± 0.05	$-0.37^{+0.10}_{-0.11}$	1.07 ± 0.12

Note.
[a] The quantities Q_{25}, Q_{50}, Q_{75} and quantile analysis itself are all defined and described in Section 3.3.

indeed we find no evidence for any source variability as indicated by that observation. Therefore, we conclude that seven sources change luminosity on a timescale corresponding to the time between the three observations (that is, over about five days from the first observation to the last).

3.5. Infrared Properties of the Discrete X-Ray Sources

The calculated *Spitzer* IRAC fluxes for the detected X-ray sources and radio sources are presented in Tables 7 and 10, respectively. We have detected counterparts to seven and six sources found inside and outside of the angular extent of NGC 45, respectively. To help interpret the colors of these sources, in Figure 4 we present a color–color scatter plot diagram of all of the detected X-ray sources that were also detected by IRAC at a statistically significant level. We have plotted the sources located within the visual extent of the galaxy as well as those sources located beyond it: two of the detected radio sources were also detected by IRAC and the measured colors of these sources are plotted as well. To help aid in the classification of the sources, we have overplotted the "Lacy wedge" (Lacy et al. 2005) that provides bounds on the colors of extragalactic sources. We find that three and four of the sources detected within and outside of the visual extent of the galaxy, respectively, have colors consistent with the extragalactic sources based on their locations within the Lacy wedge. This result is consistent with our prediction that approximately half of the detected X-ray sources seen within the visual extent of NGC 45 are actually background galaxies. Inspection of the calculated X-ray luminosities of the plotted sources reveal no obvious trends with respect to these two groups of sources (for example, the X-ray sources within the galaxy with infrared counterparts are not brighter than average).

4. THE SFR AND METALLICITY OF NGC 45

As mentioned in the introduction, the tepid SFR of NGC 45 makes it stand out compared to other nearby spiral galaxies in the local universe. NGC 45 is also known to have a low metallicity—below we discuss the metallicity of the galaxy in more detail as well as provide our own estimate of this property.

In addition to the SFR of 0.40 $M_{\odot}$ yr^{-1} for NGC 45 as measured by Lee et al. (2009) previously (which was obtained based on the ultraviolet flux measured by *GALEX*), the application of other well-known indicators of SFR also yield low SFRs for NGC 45. For example, the SFR as a function of

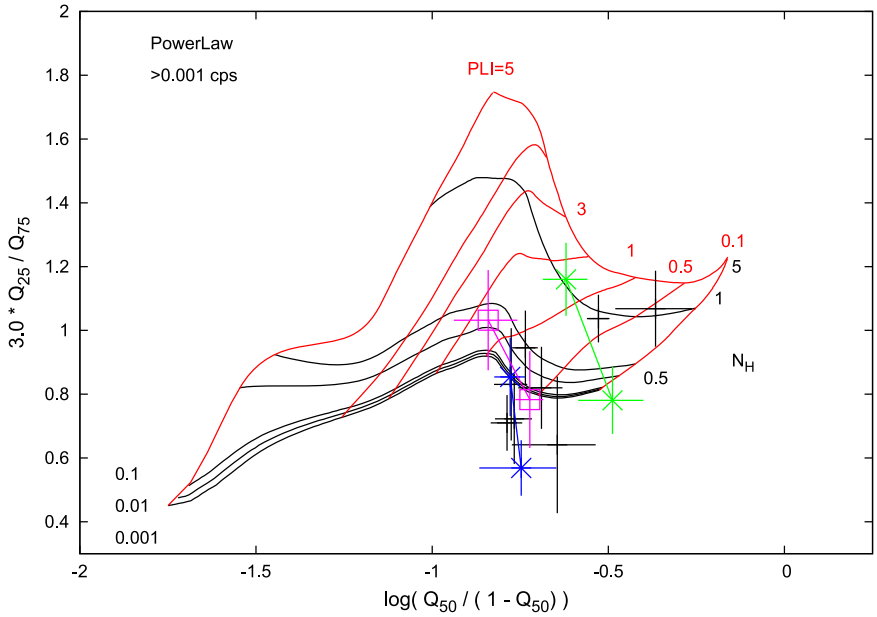

Figure 2. Quantile plot depicting the spectral properties of the detected discrete X-ray sources in NGC 45 as listed in Table 6 using a power law grid. Black crosses depict the quantiles for sources as measured from the merged observation while colored open squares show the change in measured quantiles for three sources between the ObsID 4690 and ObsID 6184 observations. The green, magenta and blue squares correspond to the sources CXOU J001406.9–230707, CXOU J001403.6–231006 and CXOU J001356.0–231240, respectively: the lines connecting the pairs of squares help show the change in measured quantiles from one observation to the other. See Section 3.3.

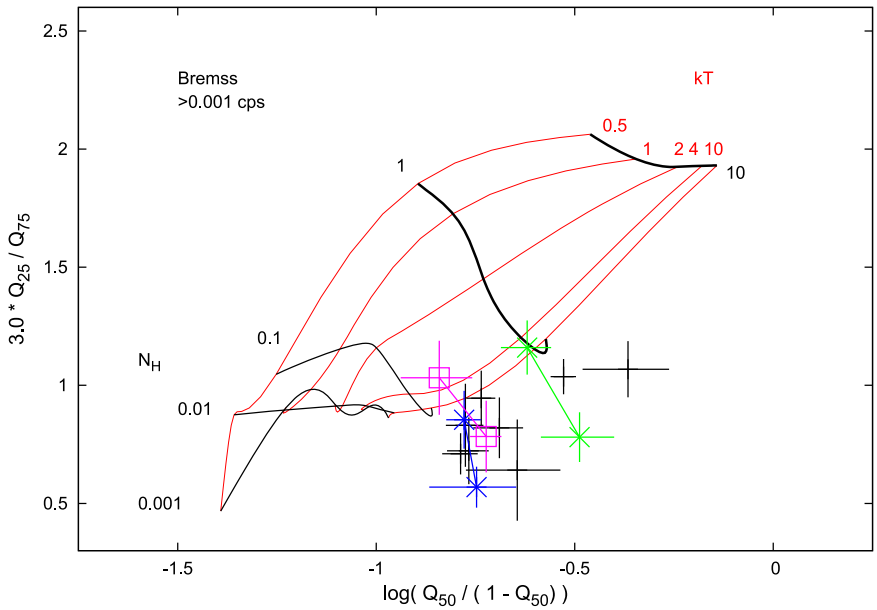

Figure 3. Same as for Figure 2 but instead a grid based on a thermal bremsstrahlung model is shown. See Section 3.3.

Hα luminosity as derived by Kennicutt (1998) can be applied: from the measured Hα flux of NGC 45 of 6.03×10^{-12} erg cm^{-2} s^{-1} (Kennicutt et al. 2008) and our adopted distance to NGC 45 of 6.6 Mpc, we calculate an Hα luminosity of $L_{\mathrm{H}\alpha} = 3.14 \times 10^{40}$ erg s^{-1}. Therefore, by applying the relation derived by Kennicutt (1998), we calculate a SFR of

$$\mathrm{SFR}\left(M_{\odot}\ \mathrm{yr}^{-1}\right) = 7.9 \times 10^{-42} L_{\mathrm{H}\alpha} = 0.24. \quad (3)$$

A second commonly implemented SFR indicator has been published by Calzetti et al. (2007) based on both $L_{\mathrm{H}\alpha}$ and $L_{24\,\mu\mathrm{m}}$, where the latter is the luminosity of NGC 45 at a wavelength of 24 μm. From the measured flux of NGC 45 at 24 μm of 0.188 Jy (Dale et al. 2009) and once again assuming a distance to NGC 45 of 6.6 Mpc, we calculate $L_{24\,\mu\mathrm{m}} = 1.22 \times 10^{41}$ erg s^{-1} and from the relation published by Calzetti et al. (2007), that is,

$$\mathrm{SFR}\left(M_{\odot}\ \mathrm{yr}^{-1}\right) = 5.3 \times 10^{-42} \times \left(L_{\mathrm{H}\alpha\ \mathrm{obs}} + \left(0.031 \pm 0.006\right) L_{24\,\mu\mathrm{m}}\right), \quad (4)$$

Table 7
IRAC Fluxes for *Chandra*-detected Discrete X-ray Sources[a]

Source	Ch 1 Match	Ch 2 Match	Ch 3 Match	Ch 4 Match	Ch 1 Flux (μJy)	Ch 2 Flux (μJy)	Ch 3 Flux (μJy)	Ch 4 Flux (μJy)
CXOU J001344.9–230856	?	?	?	?	…	…	…	…
CXOU J001347.6–230739	Yes	Yes	Yes?	Yes	48.4+/–25.4	52.6+/–26.4	64.0+/–29.6	40.6+/–23.9
CXOU J001348.4–231029	Yes	Yes	No	?	4.7Est	5.65Est	…	…
CXOU J001349.8–230857	Yes	Yes	Yes	Yes	18.6+/–15.7	33.8+/–21.9	21.1Est	15.2+/–16.8
CXOU J001354.8–230723	?	No?	No	No	…	…	…	…
CXOU J001356.0–231240	Yes	Yes	Yes	Yes	177Est	108Est	116.6+/–40.2	74.8+/–32.4
CXOU J001358.3–231107	Yes	Yes	Yes?	Yes?	6.24+/–9.12	6.56Est	5.7Est	2.49 Est
CXOU J001358.7–230639	?	?	No	No	…	…	…	…
CXOU J001400.9–231017	Yes?	Yes?	No	Yes?	4.4Est	5.95Est	…	15.47Est
CXOU J001401.2–230827	Yes	Yes	Yes	Yes	19.7+/–16.3	24.7+/–18.1	19.1Est	17.5Est
CXOU J001403.0–231218	?	No	?	?	…	…	…	…
CXOU J001403.6–231006	Yes?	Yes	?	No	22.3Est	26.7Est	…	…
CXOU J001404.1–231055[b]	Yes?	Yes?	No	No	…	…	…	…
CXOU J001404.2–230746	Yes	Yes	No	?	11.5+/–12.4	11.5+/–12.3	…	…
CXOU J001404.6–231355	Yes	Yes	Yes?	No?	13.9Est	15.5Est	19.0Est	…
CXOU J001406.1–231006	Yes	Yes	Yes	Yes	77.5+/–32.0	71.7+/–30.9	85.8+/–35.4	111.6+/–40.9
CXOU J001406.9–230707	Yes?	Yes	Yes	Yes	212.9+/–52.9	203.6+/–51.8	182.5+/–49.6	238.6+/–56.7
CXOU J001409.8–230742	Yes?	Yes	Yes	Yes?	80.3+/–32.7	82.6+/–33.1	69.5+/–31.1	4.50+/–10.4
CXOU J001410.6–230922	Yes?	Yes	Yes	Yes	123.6+/–40.5	75.4+/–31.6	33.4+/–21.6	29.9Est
CXOU J001412.8–230911	Yes	Yes	Yes	Yes	174.8 ± 48.1	145.6 ± 43.9	96.2 ± 36.6	60.2 ± 28.9
CXOU J001412.8–231111	Yes	Yes	Yes	Yes	99.3+/–36.2	40.5+/–23.1	42.2+/–24.1	18.4+/–16.7
CXOU J001413.6–230831	Yes	Yes	Yes	Yes	62.5+/–28.8	56.9+/–27.5	20.1Est	25.5+/–19.4
CXOU J001413.8–231355	?	Yes?	No	No?	3.83+/–7.27	…	…	…
CXOU J001419.7–231309	Yes	Yes	Yes	Yes	79.6+/–32.5	94.4+/–35.3	132.5+/–42.3	396.6+/–73.8
CXOU J001420.4–231235	Yes	Yes	Yes	Yes	22.4+/–17.2	19.7+/–16.1	22.3Est	20.0Est

Notes.
[a] The channels here refer to channels 1 through 4 for IRAC aboard *Spitzer*. The central wavelengths of channels 1, 2, 3 and 4 are 3.550, 4.493, 5.731 and 7.872 μm, respectively. The corresponding bandwidths of each channel are 0.750, 1.015, 1.425 and 2.905 μm, respectively. See Section 3.5.
[b] This source corresponds to the nucleus of NGC 45.

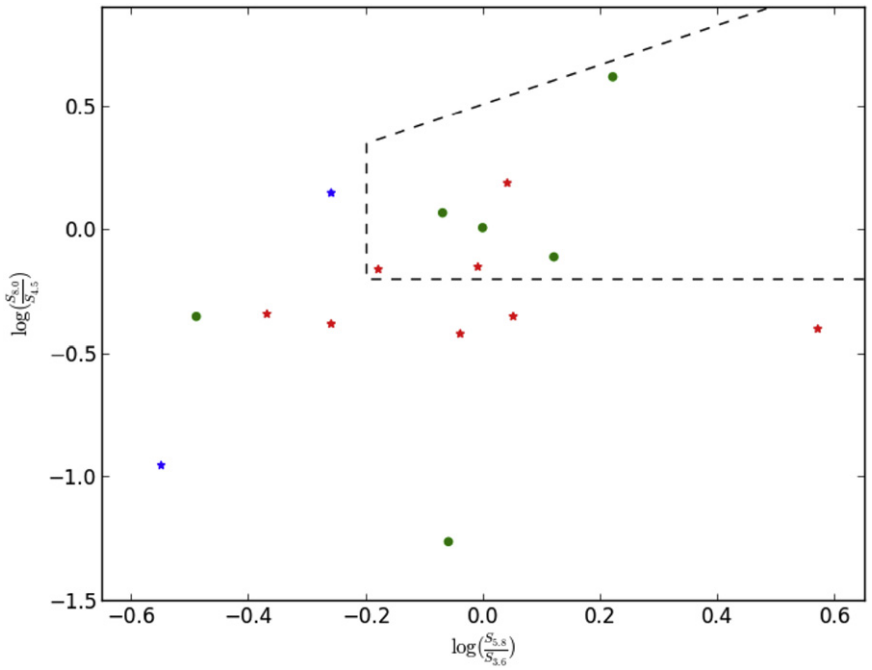

Figure 4. IRAC colors of the detected X-ray sources, based on the colors presented in Table 7. The green circles correspond to the X-ray sources located outside of the visual extent of NGC 45, the red stars correspond to the X-ray sources located within the visual extent of NGC 45 and the blue stars correspond to the radio sources detected by our radio observations that were also detected by IRAC. The dashed line indicates the location of the "Lacy wedge" (Lacy et al. 2005) that broadly defines the colors of galaxies, consistent with the interpretation that these sources are background galaxies seen in projection toward NGC 45. See Sections 3.5 and 7.

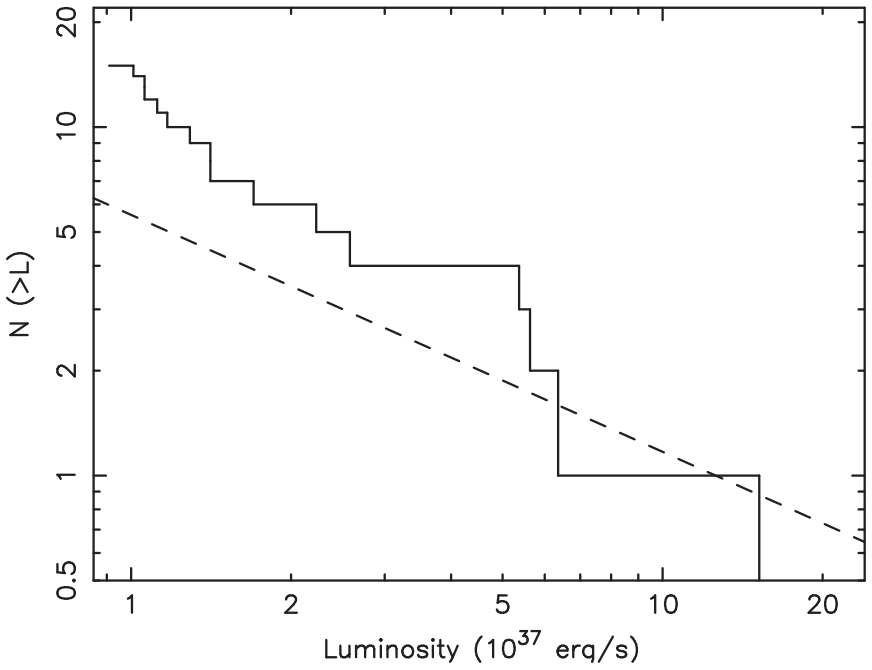

Figure 5. Cumulative X-ray luminosity function of NGC 45 (solid line) with the modeled background contribution (dashed line). See Section 5.

we obtain 0.19 $M_{\odot}$ yr^{-1}. As a third and final estimate of SFR, we apply the relation presented by Cluver et al. (2014) based on the 22 μm luminosities $L_{22\,\mu\mathrm{m}}$ of galaxies as measured by the *Wide-field Infrared Survey Explorer*. Using the measured flux density of NGC 45 at 22 μm of 227.541 mJy (kindly provided by Tom Jarrett) and once more using our adopted distance to NGC 45, we calculate $L_{22\,\mu\mathrm{m}}$ = 1.61 × 10^{41} erg s^{-1} = 4.19 × 10^{8} $L_{\odot}$. Therefore, from the relation published by Cluver et al. (2014), specifically

$$\log_{10}\mathrm{SFR}_{\mathrm{H}\alpha}\left(M_{\odot}\ \mathrm{yr}^{-1}\right) = 0.82\ \log_{10}\nu L_{22\,\mu\mathrm{m}}\ (L_{\odot}) - 7.3, \tag{5}$$

we obtain $\mathrm{SFR}_{\mathrm{H}\alpha}$ = 0.10 $M_{\odot}$ yr^{-1}. Therefore, based on all of these metrics and the previous work of Lee et al. (2009), we have established that NGC 45 does indeed have a low SFR.

The metallicity of NGC 45 is also known to be quite low based on previous studies of this galaxy. Zaritsky et al. (1994) provided metallicity estimates for galaxies as a function of Hubble type: according to Figure 10 of their paper, the metallicity of an Sd galaxy like NGC 45 is 12 + log (O/H) = 8.5. Based on analysis of observations made of the globular cluster population of NGC 45, Mora et al. (2008) measured an absorption line stellar abundance of 12 + log (O/H) = 8.5. We provide our own estimate of the metallicity of the galaxy using the relation derived by Lee et al. (2006) based on the absolute magnitude of a galaxy $M_{4.5}$ at 4.5 μm. To calculate $M_{4.5}$, we first determined $m_{4.5}$—the apparent magnitude at 4.5 μm—from the relation $m_{4.5} = -2.5\ \log_{10}(F/F_0)$, where F is the observed flux from NGC 45 at a wavelength of 4.5 μm (0.127 ± 0.017 Jy—Dale et al. 2009) and F_0 = 179.7 ± 2.6 Jy. From this relation, we calculated $m_{4.5}$ = 7.88 and from our assumed distance to NGC 45 (and assuming no extinction), we calculate $M_{4.5}$ = –21.32. Therefore, using the relation obtained by Lee et al. (2006), that is

$$12 + \log\ (\mathrm{O/H}) = 5.78 \pm 0.21 + (-0.122 \pm 0.012) M_{4.5}, \tag{6}$$

we calculate 12 + log (O/H) = 8.39 ± 0.47. For comparison purposes, we note that solar abundances have been estimated to be 12 + log (O/H) = 8.92 (Anders & Grevesse 1989) and 12 + log (O/H) = 8.69 (Wilms et al. 2000). Based on these estimates of the solar metallicities, our calculated value of the metallicity is 0.3 and 0.5 solar, respectively. All of these results underscore that NGC 45 is indeed a low metallicity galaxy.

5. THE DISCRETE X-RAY SOURCE LUMINOSITY FUNCTION OF NGC 45

In Figure 5 we present the cumulative 0.5–7.0 keV luminosity distribution of the sources within the optical extent of NGC 45. A power-law model, $N(>L) = N_0 L_{37}^{\Gamma}$, plus a similar component representing the background, $N(>L) = 5.6 L_{37}^{-0.68}$ (see Equation (1); shown as the dashed curve in Figure 7), was fit to the distribution by minimizing the likelihood function. The best-fit slope is $\Gamma = -1.3^{+0.7}_{-1.6}$ and normalization is $N_0 = 8.0^{+3.5}_{-2.6}$ (the quoted errors correspond to 90% confidence limits). Here $N(>L)$ is the number of sources with X-ray luminosity exceeding L and $L = 10^{37} L_{37}$ is the 0.5–7.0 keV luminosity. Fits with more complex models including a broken power law and an exponentially cutoff power law produce similar results with no improvement in the quality of the fit.

This slope is much steeper than (but within 1σ of) the universal value of ∼ −0.6 derived for star-forming galaxies by Grimm et al. (2003) and, more recently, by Mineo et al. (2012). The normalization was found in those studies to be directly proportional to the global SFRs of the host galaxies, provided the X-ray point source population is

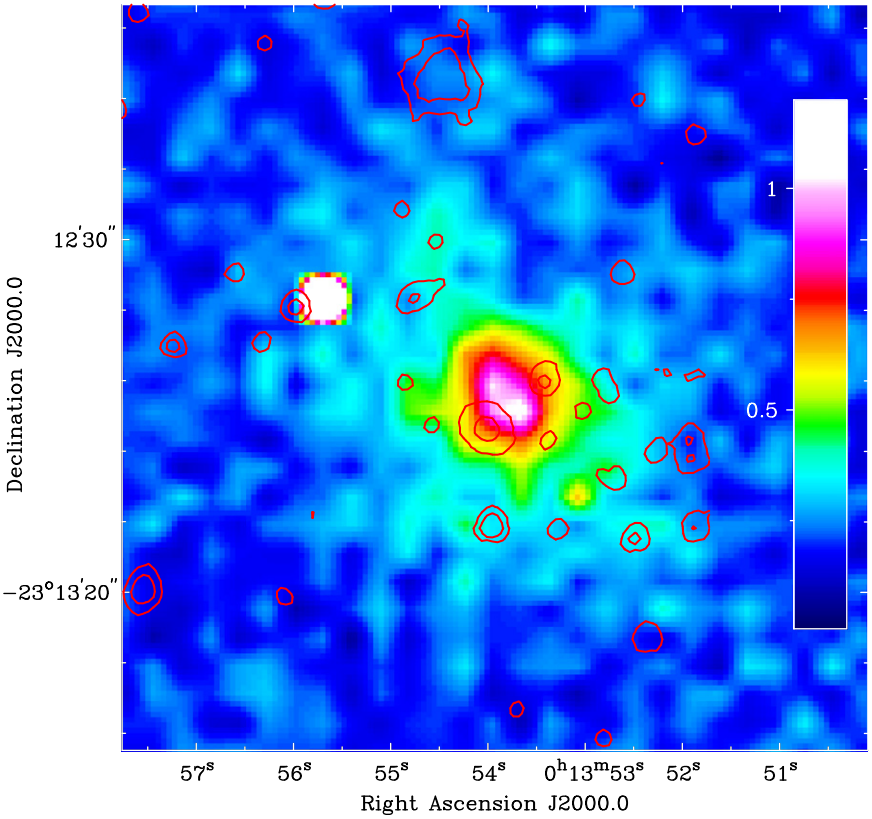

Figure 6. *Chandra* image of the background galaxy cluster CXOU J001354.2-231254.7 with contours showing IRAC emission overlaid depicting emission detected by IRAC at Channel 1 (3.6 μm). The contours are placed at the levels of 0.22 and 0.57 MJy/sr and the color scale is in counts s^{-1} $pixel^{-1}$, where one square pixel corresponds to $0''.5 \times 0''.5$. See Section 6.

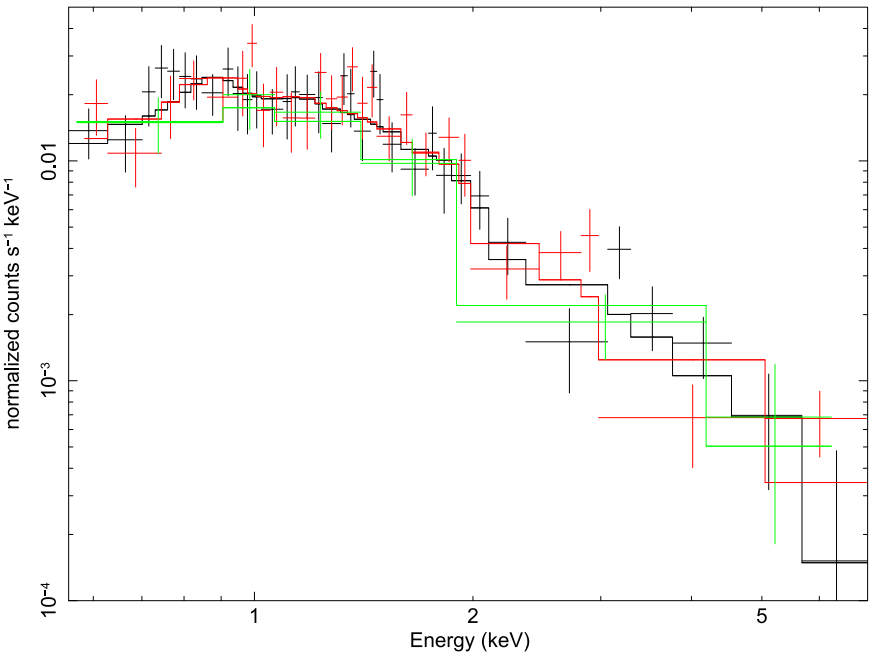

Figure 7. Extracted *Chandra* ACIS spectra from the background galaxy cluster CXOU J001354.2–231254.7. The black, red and green spectra were extracted from ObsIDs 4690, 6184 and 6185, respectively. The spectra are fit with a PHABS × APEC model with variable redshift. See Section 6 and Table 8.

dominated by young accreting binary systems with high-mass donor stars. This may be the case for NGC 45 since it is a late-type spiral. However, it has a low to moderate SFR and a moderate mass so that contributions from low-mass X-ray binaries are also expected. Scaling the expression from Grimm et al. (2003) to our limiting flux of

Table 8
Fit Parameters and Calculated Properties of Galaxy Cluster CXOU J001353.9–231258.3[a]

Property	CXOU J001354.2–231254.7
$N_{\rm H}$ ($\times 10^{22}$ cm^{-2})	0.07 (<0.14)
kT (keV)	$4.22^{+2.08}_{-1.42}$
Abundance[b]	0.30 (<0.75)
Redshift z	0.28 ± 0.14
Normalization[c] (cm^{-5})	2.52(±0.72) × 10^{-4}
$\Delta\chi^2$ (χ^2/Degrees of Freedom)	0.95 (107.93/114)
Hydrogen Number Density $n_{\rm H}$ (cm^{-3})	4(±1) × 10^{-3}
Abosorbed Flux[d] (erg cm^{-2} s^{-1})	1.75 × 10^{-13}
Unabsorbed Flux[d] (erg cm^{-2} s^{-1})	1.98 × 10^{-13}
Unabsorbed Luminosity[d] (erg s^{-1})	8.77(±0.96) × 10^{43}
X-ray Emitting Mass ($M_\odot$)	2.32(±1.75) × 10^{12}

Notes.
[a] All quoted error bounds correspond to 90% confidence intervals. A value for Hubble's constant of $H_0 = 67 \pm 1.2$ km s^{-1} Mpc^{-1} has been assumed throughout the calculations. See Section 6 for a discussion of the general properties of this cluster.
[b] Relative to solar.
[c] Defined as $(10^{-14}/4\pi(d_{\rm L}(1+z))^2)\int n_{\rm e} n_{\rm H} dV$, where $d_{\rm L}$ is the luminosity distance to the cluster in cm, z is the redshift, $n_{\rm e}$ is the electron number density in cm^{-3}, $n_{\rm H}$ is the proton number density in cm^{-3} and $V = \int dV$ is the total volume of the X-ray emitting gas. See Section 6.
[d] For the energy range 0.5–7.0 keV.

$L_{37} \sim 1$, we expect $N_0 = 21.8 \times$ SFR or from 2.2 to 8.7 high-mass X-ray binaries based on the SFR estimates derived above. This is roughly consistent with the net numbers of observed sources.

The slope is also consistent with the low-luminosity slope, $\Gamma = -0.7$ to -1.2, observed from populations of older low-mass X-ray binaries in early-type galaxies (Kim & Fabbiano 2004) though their luminosity functions often show breaks within our luminosity range (e.g., Gilfanov 2004; Kim et al. 2006) making it difficult to make a direct comparison to our results.

6. CXOU J001354.2–231254.7: A NEW X-RAY DETECTED GALAXY CLUSTER

The *Chandra* observations detected X-ray emission from a background galaxy cluster seen toward the southwest outside of the angular extent of NGC 45. The coordinates of the center of the cluster are R.A. (J2000.0) $00^{\rm h}13^{\rm m}54^{\rm s}.2$, decl.(J2000.0) $-23°12'54''.7$: therefore, we will refer to this cluster as CXOU J001354.2–231254.7 for the remainder of this paper. This source was first identified as RX J001353.6–231318 in the *ROSAT* All Sky Survey Faint Source Catalog (Voges et al. 2000): it was also detected and cataloged as source X20 in the previously published catalog of sources detected by *Chandra* toward NGC 45 by Liu (2011). In Figure 6 we present a broadband *Chandra* image of CXOU J001354.2-231254.7 with contours overlaid to depict emission detected by IRAC at Channel 1 (3.6 μm). To investigate the spectral properties of this cluster, we used `specextract` to extract source and background spectra along with auxiliary response functions and redistribution matrix files from all three observations. The radius of the source extraction region was 40 arcsec: the background extraction region was an annular region centered on the source region with a radius of 60 arcsec. The source extraction region also excluded flux from the discrete source CXOU J001356.0–231240 to reduce the presence of contaminating flux from unrelated sources in the extracted spectra of the cluster.

The extracted spectra were fitted using the XSPEC software package Version 12.8.1g (Arnaud 1996). The thermal APEC model[17] was used to model the thermal diffuse emission from the cluster and the abundance parameter (describing elemental abundances relative to solar) and the redshift were allowed to vary. Finally, the APEC model was combined with the photoelectric model PHABS to account for photoelectric absorption along the line of sight. While fitting, a statistically acceptable fit (χ^2/degrees of freedom = 107.93/114 = 0.95) was obtained with the APEC model: in Table 8 we present a summary of the parameters of this fit. In Figure 7 we present the extracted *Chandra* ACIS spectra for this cluster as fit with the APEC model. Based on the fitted redshift ($z = 0.28 \pm 0.14$) and assuming a value for Hubble's Constant of $H_0 = 67 \pm 1.2$ km s^{-1} Mpc^{-1} (Ade et al. 2015), we determined the angular size distance, luminosity distance $d_{\rm L}$ and comoving radial distance to the cluster using the on-line Cosmology Calculator created by Ned Wright[18] of 4.447 kpc/″, 1503 and 1174 Mpc, respectively, assuming a matter density $\Omega_{\rm M}$= 0.286 and a vacuum energy density $\Omega_{\rm vac} = 0.714$. At this distance, the angular radius of our extraction region of 40 arcsec corresponds to a linear radius of $r = 178$ kpc. The unabsorbed flux S_X measured from the cluster over the energy range of 0.5–7.0 keV is 1.98×10^{-13} erg cm^{-2} s^{-1}. To calculate the unabsorbed X-ray luminosity L_X of CXOU J001354.2–231254.7 over this energy range, we use the relation

$$L_X = 4\pi\left(d_{\rm L}(1+z)\right)^2 S_X, \quad (7)$$

which yields $L_X = 8.77 \times 10^{43}$ erg s^{-1} over the energy range 0.5–7.0 keV. The definition of the normalization parameter for the APEC model is

$$\text{Normalization} = \frac{10^{-14}}{4\pi\left(d_{\rm L}(1+z)\right)^2}\int n_{\rm e} n_{\rm H} dV, \quad (8)$$

where $n_{\rm e}$ and $n_{\rm H}$ are the electron and hydrogen number densities in cm^3, respectively, and $V = \int dV$ is the volume of the X-ray emitting gas (assumed to be spherical and calculated to be $V = (4/3)\pi r^3 = 6.94 \times 10^{71}$ cm^3). From the normalization of the fit and assuming that $n_{\rm H}$ and $n_{\rm e}$ are uniform throughout the volume of the X-ray emitting plasma and that $n_{\rm H} = n_{\rm e}$, we calculate $n_{\rm H} = n_{\rm e} = 4(\pm 1) \times 10^{-3}$ cm^{-3}. Finally, from the estimated volume of the X-ray emitting plasma, we calculate the mass of the X-ray emitting gas to be $M = 2.32(\pm 1.75) \times 10^{12} M_\odot$.

7. RADIO RESULTS

Six radio sources were identified at 6 cm and no sources were detected at 20 cm. The 20 cm image has a rms sensitivity that is three times higher than the 6 cm image. This means that flat-spectrum sources that are detected at 6 cm would not be detectable in the 20 cm image. Sources previously identified by

[17] Corresponding to an emission spectrum from a collisionally ionized diffuse gas calculated using the atomic database (ATOMDB) code. See http://atomdb.org/.
[18] http://www.astro.ucla.edu/~wright/CosmoCalc.html—also see Wright (2006).

Table 9
Properties of Discrete Radio Sources Observed Toward NGC 45[a]

ID	R.A. (J2000.0) (h m s)	Decl. (J2000.0) (° ′ ″)	$S_{6\,cm}$ (mJy)	α	Notes	Counterpart
45-R1	00:13:46.7	–23:13:10.7	0.40 ± 0.15	0.44 ± 0.18	⋯	⋯
45-R2	00:13:47.3	–23:14:21.0	1.46 ± 0.13	1.51 ± 0.12	extended	MRSS 472–003130
45-R3	00:13:50.4	–23:13:34.6	1.07 ± 0.51	1.26 ± 0.21	double-peak?	⋯
45-R3a	00:13:50.5	–23:13:34.4	0.40 ± 0.09	0.44 ± 0.14	⋯	⋯
45-R4	00:13:52.3	–23:13:29.9	0.51 ± 0.16	0.64 ± 0.16	⋯	MRSS 473–114430
45-R5	00:14:06.7	–23:08:59.6	0.15 ± 0.11	–0.39 ± 0.29	Weak	⋯
45-R6	00:14:22.2	–23:07:59.7	0.13 ± 0.11	–0.46 ± 0.31	Weak	⋯

Note.
[a] Counterparts identified using a 5 arcsec search radius. MRSS—background galaxy detected by the Muenster Red Sky Survey (Ungruhe et al. 2003). See Section 7.

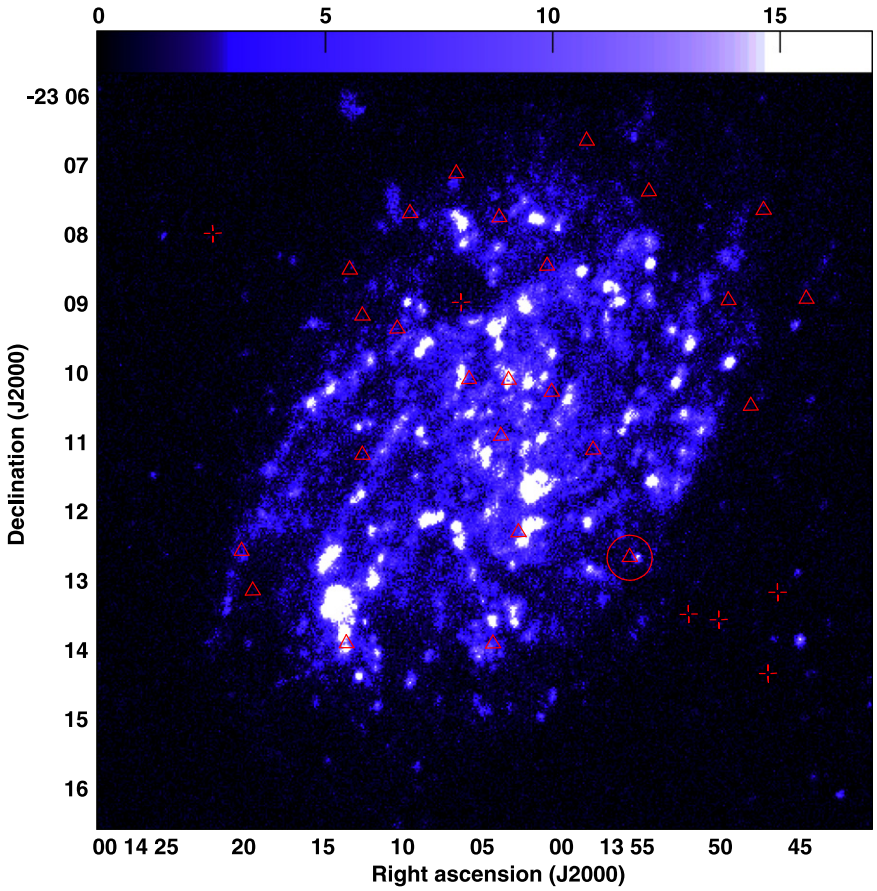

Figure 8. Ultraviolet image of NGC 45 from *GALEX*. The scale of the image is from 0 to 17 mJy. The locations of the discrete radio sources are indicated with crosses while the locations of the detected X-ray sources are indicated with triangles. The circle indicates the position of the detected X-ray galaxy cluster CXOU J001354.2–231254.7, which is discussed in Section 6. For more information about the detected radio sources, see Section 7.

the NRAO VLA Sky Survey (see Condon et al. 1988) were detectable outside of NGC 45. The source R45-R3 may be a double-peaked source but the second peak is right at the detection limit.

We have used a 3σ upper limit for the 20 cm flux density based on the rms sensitivity of 78 μJy/beam for the 20 cm radio map. In Table 9 we present measured flux densities at 6 cm for the detected sources, as well as spectral index α measurements[19], notes about the morphology and intensities of each source and finally the search for counterparts from previously published works. We find that two radio sources —R2 and R4—have been previously detected as sources MRS 472-003130 and MRS 473-114430, respectively, by the Muenster Red Sky Survey (Ungruhe et al. 2003). We find no X-ray counterparts to any of the detected radio sources. In Figure 8 we present an ultraviolet image of NGC 45 with the locations of the detected discrete radio sources indicated. A cluster of four discrete radio sources seen toward the southeast of the galaxy may correspond to a background cluster of galaxies: the spectral indices of these

[19] Here, we have adopted the convention $S_\nu \propto \nu^{-\alpha}$.

Table 10
IRAC Fluxes for Discrete Radio Sources[a]

ID	R.A. (J2000.0)	Decl. (J2000.0)	Ch 1 Match	Ch 2 Match	Ch 3 Match	Ch 4 Match	Ch 1 Flux (μJy)	Ch 2 Flux (μJy)	Ch 3 Flux (μJy)	Ch 4 Flux (μJy)
45-R1	00:13:46.7	−23:13:10.7	No	No	No	No	⋯	⋯	⋯	⋯
45-R2	00:13:47.3	−23:14:21.0	Yes	Yes	Yes	Yes	27.1 ± 5.21	16.9 ± 4.1	7.6 ± 2.8	1.9 ± 1.4
45-R3	00:13:50.4	−23:13:34.6	No	No	No	No	⋯	⋯	⋯	⋯
45-R3a	00:13:50.5	−23:13:34.4	No	No	No	No	⋯	⋯	⋯	⋯
45-R4	00:13:52.3	−23:13:29.9	No	No	No	No	⋯	⋯	⋯	⋯
45-R5	00:14:06.7	−23:08:59.6	No	No	No	No	⋯	⋯	⋯	⋯
45-R6	00:14:22.2	−23:07:59.6	Yes	Yes	Yes	Yes?	14.3 ± 3.8	9.6 ± 3.1	7.9 ± 2.8	13.6Est

Note.
[a] Definitions of the IRAC channels are the same as those presented in Table 7. See Section 7.

sources are consistent with galaxies. The association of these galaxies with the cluster CXOU J001354.2–231254.7 discussed in the previous section is uncertain due to the large position offset between these radio sources and the observed diffuse emission of the cluster. Of the two remaining sources (which were weakly detected compared to the previous four sources), one—45-R5—is detected within the visual extent of NGC 45: its location within the galaxy and its measured spectral index (consistent with a synchrotron origin) suggest that it may be a SNR, but no X-ray counterpart is seen and additional observations are required to investigate the classification of this source in a more rigorous manner. The remaining source—45-R6—also has a spectral index consistent with a synchrotron origin but its location outside of the visual extent of the galaxy makes a classification as a SNR less likely. The true nature of this source is also uncertain.

We measured *Spitzer* IRAC fluxes of the detected radio sources: two sources were also detected by *Spitzer* and then fluxes for these sources are presented in Table 10. We have plotted the positions of these sources in Figure 4.

8. CONCLUSIONS

The conclusions of our paper may be summarized as follows.

1. We present an analysis of three archival *Chandra* observations of the nearby spiral galaxy NGC 45. The total combined effective exposure time of the three observations is 63515 s. A total of 25 discrete X-ray sources are found in the entire field of view of the ACIS-S3 chip and 16 sources are found within the visual extent of the galaxy. The limiting unabsorbed luminosity of the merged observation is $\sim 10^{37}$ erg s^{-1} over the energy range 0.5–7.0 keV.
2. We have searched for counterparts at other wavelengths for these sources: we identify associations between one X-ray source and a resident star cluster as well as an association between an X-ray source and a background galaxy. We find no X-ray counterparts to Galactic foreground stars seen toward NGC 45 and we estimate that about half of the sources in the entire field of view and half of the sources seen within the visual extent of the galaxy may be background sources.
3. To aid in classifying the sources based on their spectral properties, we have also performed a quantile analysis as well for those sources detected with a sufficient number of counts for at least a basic quantile analysis. Based on the calculated quantiles for these sources and their locations on interpretive grids, it appears that the majority of the brightest X-ray sources are either candidate X-ray binaries or background AGNs.
4. We have searched for time variability in the X-ray emission from the discrete X-ray sources during the three individual X-ray observations. One source is seen to be variable during the ObsID 4690 observation: it may be associated with a background galaxy or an X-ray binary associated with NGC 45. When comparing luminosity estimates of discrete sources from one observation epoch to another, we find that seven X-ray sources appear to vary in luminosity by a detectable amount between the observations (covering a time span of approximately five days).
5. We have measured the *Spitzer* IRAC fluxes of the *Chandra*-detected sources from our observations of NGC 45: we have detected infrared counterparts to seven and six sources found inside and outside of the visual extent of the galaxy, respectively. A scatter plot of the infrared colors of these sources shows that the sources found outside of the galaxy have infrared colors consistent with background galaxies.
6. We have applied several different methods to estimate the SFR of NGC 45: these methods all return values of ∼0.20 $M_{\odot}$ yr^{-1}. Similarly, we have estimated the metallicity of NGC 45 to be 12 + log (O/H) = 8.39 ± 0.47. Our calculated values for the SFR and the metallicity are consistent with values published previously in the literature.
7. We have estimated the slope of the luminosity function of the discrete X-ray source population of NGC 45 (when taking into account the presence of background galaxies) to be $\Gamma = -1.3^{+0.7}_{-1.6}$. This slope is steeper but within 1σ of the universal value of –0.6 derived for star-forming galaxies.
8. We have conducted a detailed spectral analysis of the diffuse hot gas associated with a background galaxy cluster (CXOU J001354.2–231254.7) that has been detected by these observations. Our fit parameters to the extracted ACIS spectra of the gas are a column density $N_{\rm H} = 0.07(<0.14) \times 10^{22}$ cm^{-2}, a temperature $kT = 4.22^{+2.08}_{-1.42}$ keV, an abundance $Z = 0.30(<0.75)$ relative to solar and a redshift $z = 0.28 \pm 0.14$. From the fit parameters we derive an electron number density $n_{\rm e} = 4(\pm 1) \times 10^{-3}$ cm^{-3}, an unabsorbed X-ray luminosity $L_{0.5-7.0\,\rm keV} \sim 8.77(\pm 0.96) \times 10^{43}$ erg s^{-1} for the

cluster and an X-ray emitting mass $M = 2.32 (\pm 1.75) \times 10^{12} M_{\odot}$.

9. We have also presented radio continuum observations of NGC 45. A total of six discrete radio sources have been detected: we find no X-ray counterparts to any of these sources. Based on spectral analysis of the radio sources, complementary analysis of their IRAC fluxes (for the two radio sources with infrared counterparts detected by IRAC) and consideration of their locations as seen with respect to the angular extent of NGC 45, we conclude that one source is a candidate radio SNR while the remaining sources are likely to be background galaxies unrelated to NGC 45.

We thank the anonymous referee for many helpful comments that greatly improved the quality of this paper. T. G. P. thanks Daniela Calzetti, Leslie Hunt, Tom Jarrett and Mark Lacy for useful discussions about the star formation rate and the metallicity of NGC 45. T. G. P. also thanks Daniel Clay Graves for his assistance in reducing the *Chandra* observations of NGC 45. T. G. P. is also grateful to the NRAO for providing sabbatical support as a visiting scientist at the Domenici Science Operations Center in Socorro, New Mexico, during which much of this paper was written. This research has made use of NASA's Astrophysics Data System and the NASA/IPAC Extragalactic Database (NED) which is operated by the Jet Propulsion Laboratory, California Institute of Technology, under contract with the National Aeronautics and Space Administration. This work is based in part on archival data obtained with the *Spitzer Space Telescope*, which is operated by the Jet Propulsion Laboratory, California Institute of Technology under a contract with NASA.

Facilities: Chandra (ACIS), *Spitzer* (IRAC), VLA

REFERENCES

Ade, P. A. R., Aghanim, N., Arnaud, M., et al. 2015, A&A, 580, A22
Anders, E., & Grevesse, N. 1989, GeCoA, 53, 197
Arnaud, K. A. 1996, in ASP Conf. Ser. 101, Astronomical Data Analysis Software and Systems V, ed. G. Jacoby & J. Barnes (San Francisco, CA: ASP), 17
Bertin, E., & Arnouts, S. 1996, A&AS, 117, 393
Blair, W. P., & Long, K. S. 1997, ApJS, 108, 261
Blair, W. P., & Long, K. S. 2004, ApJS, 155, 101
Calzetti, D., Kennicutt, R. C., Jr., Engelbracht, C. W., et al. 2007, ApJ, 666, 870
Campana, S., Moretti, A., Lazzati, D., & Tagliaferri, G. 2001, ApJL, 560, L19
Chemin, L., Carignan, C., Drouin, N., & Freeman, K. C. 2006, AJ, 132, 2527
Cluver, M. E., Jarrett, T. H., Hopkins, A. M., et al. 2014, ApJ, 782, 90
Condon, J. J., Cotton, W. D., Greisen, E. W., et al. 1998, AJ, 115, 1693
Crampton, D., Gussie, G., Cowley, A. P., & Schmidke, P. C. 1997, AJ, 114, 2353
Dale, D. A., Cohen., S. A., Johnson, L. C., et al. 2009, ApJ, 703, 517
Dodorico, S., Dopita, M. A., & Benvenuti, P. 1980, A&AS, 40, 67
Evans, I. N., Primini, F. A., Glotfelty., K. J., et al. 2010, ApJS, 189, 37
Fabbiano, G. 2006, ARA&A, 44, 323
Fazio, G. G., Hora, J. L., Allen, L. E., et al. 2004, ApJS, 154, 10
Foster, A. R., Ji, L., Smith, R. K., & Brickhouse, N. S. 2012, ApJ, 756, 128
Freeman, P. E., Kashyap, V., Rosner, R., & Lamb, D. Q. 2002, ApJS, 138, 185
Fruscione, A., McDowell, J. C., Allen, G. E., et al. 2006, Proc. SPIE, 6270, 62701V
Garmire, G. P., Bautz, M. W., Ford, P. G., Nousek, J. A., & Ricker, G. R., Jr. 2003, Proc. SPIE, 4851, 28
Gilfanov, M. 2004, MNRAS, 349, 146
Gregory, P. C., & Loredo, T. J. 1992, ApJ, 398, 146
Grimm, H.-J., Gilfanov, M., & Sunyaev, R. 2003, MNRAS, 339, 793
Hong, J., Schlegel, E. M., & Grindlay, J. E. 2004, ApJ, 614, 508
Jacobs, B. A., Rizzi, L., Tully, R. B., et al. 2009, AJ, 138, 332
Karachentsev, I. D., & Kaisinia, E. I. 2013, AJ, 146, 46
Karachentsev, I. D., Makarov, D. I., & Kaisina, E. I. 2013, AJ, 145, 101
Kennicutt, R. C., Jr. 1998, ARA&A, 36, 189
Kennicutt, R. C., Jr., Lee, J., Funes, S., et al. 2008, ApJS, 178, 247
Kim, D.-W., & Fabbiano, G. 2004, ApJ, 611, 846
Kim, D.-W., Fabbiano, G., Kalogera, V., et al. 2006, ApJ, 652, 1090
Lacy, M., Wilson, G., Masci, F., et al. 2005, ApJS, 161, 41
Lee, H., Skillman, E. D., Cannon, J. M., et al. 2006, ApJ, 647, 970
Lee, J. C., Gil de Paz, A., Tremonti, C., et al. 2009, ApJ, 706, 599
Liu, J. 2011, ApJS, 192, 10
Long, K. S., Blair, W. P., Winkler, P. F., et al. 2010, ApJS, 187, 495
Long, K. S., Kuntz, K. D., Blair, W. P., et al. 2014, ApJ, 212, 21
Markevitch, M., Bautz, M. W., Biller, B., et al. 2003, ApJ, 583, 70
Matonick, D. M., & Fesen, R. A. 1997, ApJS, 112, 49
Mineo, S., Gilfanov, M., & Sunyaev, R. 2012, MNRAS, 419, 2095
Mora, M. D., Larsen, S. S., & Kissler-Patig, M. 2008, A&A, 489, 1065
Pannuti, T. G., Duric, N., Lacey, C. K., et al. 2000, ApJ, 544, 780
Pannuti, T. G., Duric, N., Lacey, C. K., et al. 2002, ApJ, 565, 966
Pannuti, T. G., Schlegel, E. M., Filipovic, M., et al. 2011, AJ, 142, 20
Pannuti, T. G., Schlegel, E. M., & Lacey, C. K. 2007, AJ, 133, 1361
Pence, W. D., Snowden, S. L., Mukai, K., & Kuntz, K. D. 2001, ApJ, 561, 189
Schlegel, E. M., & Pannuti, T. G. 2003, AJ, 125, 3025
Silva-Villa, E., & Larsen, S. S. 2011, A&A, 529, 25
Smith, R. K., Brickhouse, N. S., Liedahl, D. A., & Raymond, J. C. 2001, ApJL, 556, L91
Soria, R., & Wu, K. 2003, A&A, 410, 53
Terashima, Y., & Wilson, A. S. 2004, ApJ, 601, 735
Tuellmann, R., Gaetz, T. J., Plucinsky, P. P., et al. 2011, ApJS, 193, 31
Tully, R. 1988, Nearby Galaxies Catalog (Cambridge: Cambridge Univ. Press)
Ungruhe, R., Seitter, W. C., & Duerbeck, H. W. 2003, JAD, 9, 1
Voges, W., Aschenbach, B., Boller, T., et al. 2000, IAU Circ., 7432, 1
Weisskopf, M. C., Brinkman, B., Canizares, C., et al. 2002, PASP, 114, 1
Werner, M. W., Roellig, T. L., Low, F. J., et al. 2004, ApJS, 154, 1
Wilms, J., Allen, A., & McCray, R. 2000, ApJ, 542, 914
Wright, E. L. 2006, PASP, 118, 1711
Zaritsky, D., Kennicutt, R. C., Jr., & Huchra, J. P. 1994, ApJ, 420, 87